Progress In Electromagnetics Research B, Vol. 45, 57–82, 2012

A PARTIAL COHERENT PHYSICAL MODEL OF THIRD AND FOURTH STOKES PARAMETERS OF SASTRUGI SNOW SURFACES OVER LAYERED MEDIA WITH ROUGH SURFACE BOUNDARY CONDITIONS OF CONICAL SCATTERING COMBINED WITH VECTOR RADIATIVE TRANSFER THEORY

W. Chang* **and L. Tsang**

Department of Electrical Engineering, University of Washington, Seattle, WA 98195, USA

Abstract—In this paper, a partial coherent approach is used to study the third and fourth Stokes parameters in passive microwave remote sensing of Sastrugi snow surface over layered snow structures. The incoherent part of the model consists of using radiative transfer theory for the snow layers. The coherent part of the model is using numerical solutions of Maxwell equations to derive the bistatic scattering and transmission coefficients of conical scattering by sastrugi surfaces which have large heights and large slopes. We then use the rough surface boundary conditions of conical scattering from the coherent part, in the incoherent radiative transfer equations. The radiative transfer equations are then solved iteratively that includes multiple interactions between the layered structures and the rough surfaces. Simulation results indicate that large third and fourth Stokes parameters are obtained because of the coupling of large angle transmissions of the rough surfaces with the internal reflections of layered structures. The partial coherent approach also eliminates the coherent interference patterns in angular variations from multiple reflections of layer boundaries that were present in the fully coherent approach.

1. INTRODUCTION

WindSat satellite carries the first space-borne polarimetric radiometer that measures all four Stokes parameters, i.e., the vertical

Received 15 August 2012, Accepted 9 October 2012, Scheduled 24 October 2012

* Corresponding author: Wenmo Chang (wmchang@u.washington.edu).

polarized brightness temperatures, the horizontal polarized brightness temperatures, and the real and imaginary part of the cross-correlations of the vertical and horizontal polarizations [1]. It was launched in 2003, and its observations covered a large area of ocean surfaces, ice sheets and land. The surprising measurement results were the large third and fourth Stokes parameters for both X-band (10.7 GHz) and K-band (18.7 GHz) over Greenland and Antarctica [1]. These areas are characterized by anisotropic Sastrugi surfaces that are over multilayer snow structures. The Sastrugi surfaces are wind-induced and have preferred directions in the horizontal plane. In addition to these wind induced anisotropy in the rough surfaces, Sastrugi surfaces have large RMS heights compared with the wavelengths at X band and K band. They also have large slopes. The multilayer snow structures are the consequences of snow accumulation patterns. The polarimetric signature over Greenland area is of particular interest. Specifically in spring season, the third and fourth Stokes parameters can be up to 20 K. Previously, the airborne and space borne measurements of third and fourth Stokes were not of such large magnitudes. Measurements over ocean give fourth Stokes parameter that is close to zero [2]. Theoretical predictions also give small fourth Stokes parameters for ocean thermal emission [3].

It was first derived by Tsang [4, 5], using vector radiative transfer theory and rough surface scattering, that azimuthal asymmetry can create nonzero third and fourth Stokes parameters. Therefore, these two Stokes parameters can be considered as containing anisotropic information of the medium. From the temporal aspect, the seasonal variations of the third and fourth Stokes parameters can be correlated with the seasonal geophysical changes in the snow structure. In previous theoretical research [5], large fourth Stokes parameters can be the results of volume scattering of non-spherical particles. To show the possibility of large fourth Stokes parameters, recently we have used the model of anisotropic rough surfaces with large slopes and large heights over layered media [6]. In that paper, emissivity of all four Stokes parameters were considered, using a complete fully coherent approach of rough surface scattering from a periodic surface over layered medium. The multilayer medium effects are accounted coherently by using the multilayer Green's functions. However, because of the coherent nature of the approach, the coherent multiple scattering from periodic surfaces and the coherent interferences of multiply reflected waves from the layered media exhibit significant angular fluctuations of all four Stokes parameters. The multilayers actually have random layer thicknesses. Thus an incoherent radiative transfer approach can be preferred over a coherent layered medium approach.

Thus we proposed a partial coherent approach in a previous paper [7] to study the first two Stokes parameters. In the first step of that paper [7], we study the bistatic reflection and transmission properties of random rough Sastrugi surface with large slope and large height by solving surface integral equations. In the second step, the bistatic reflective and transmission properties of the random rough surfaces are used as boundary conditions for the radiative transfer equations over layered media. However, in that paper [7], only a 2D problem is considered with the incident wave in the plane of the rough surface. Thus only the first two Stokes parameters, viz., the vertical and horizontal brightness temperatures were studied. The third and fourth Stokes parameters were not studied because they are zero for the 2D problems in that previous paper [7].

In this paper, to study the case of nonzero third and fourth Stokes parameters, we extend the partial coherent approach in [7] to the 3D problem of conical diffraction by random Sastrugi surfaces. Using surface integral equations, the 3D bistatic reflection and transmission 4 by 4 matrices were derived for the 4 Stokes parameters. Because Sastrugi surfaces [8] have large heights and large slope, method of moment is used in the studies instead of the T-matrix method used in previous studies [9, 10], because the T-matrix method or the extended boundary condition method are limited to small slopes and small to moderate heights. The 4 by 4 reflection and transmission bistatic matrices are then used in the boundary conditions of the vector radiative transfer equations of 4 Stokes parameters [11] for multi-layered snow. The approach is labeled partially coherent because the rough surfaces bistatic properties are computed by full wave solutions of Maxwell equations which are coherent solutions while the layered media part are solved by incoherent vector radiative transfer equation. The partial coherent approach has smooth angular dependence when compared with the previous fully coherent approach [6]. The vector radiative transfer equations are solved iteratively. Numerical results of the approach are compared with the fully coherent approach. Numerical results are illustrated for various roughness profiles over multilayered structures. The results show that the third and fourth Stokes parameters are significant for both X-band (10.7 GHz) and K-band (18.7 GHz). They are particularly large when the Sastrugi surfaces and multilayer snow structures exist.

In Section 2, we described the surface generation of random Sastrugi surfaces. In Section 3, we describe the surface integral equations for solving the reflective and transmission 4 by 4 matrices in conical scattering. Results of bistatic scattering and transmission matrices are illustrated for incidence from air to snow and also from

snow to air. In Section 4, we describe the vector radiative transfer equations with bistatic rough surface boundary conditions for the 4 Stokes parameters. The computed numerical results of Section 3 are used to implement the rough surface boundary conditions. The iterative approach of solving vector radiative equations with rough surface boundary conditions is described. In Section 5, the results of 4 Stokes parameters are illustrated for various geometries representative of Greenland ice sheets.

2. COMPUTER GENERATION OF RANDOM SASTRUGI SURFACES

The main features of the snow structures in Greenland area include Sastrugi surfaces and multilayer snow packs. Sastrugi surface is a wind induced snow surface, and is randomly rough surface with ridges. Figure 1 shows a typical profile of the rough surface, and the underlying snow layered structure is also included in the figure. Within a certain area, the wind induced snow surface has only 1-D roughness, so the scattering problem can be modeled as an 1-D rough surface $z = f(x)$ and conical incident and scattering waves $\phi_i \neq 0,\ \phi_s \neq 0$.

The Sastrugi surface has large height of the order of 20 cm (which is 7.1 wavelengths at 10.7 GHz), and large slope up to 75° [8]. The multilayer snow structures in Polar Regions and in Greenland are due to snow density fluctuations which are consequences of the snow accumulation pattern. Thus each layer has a distinct dielectric constant depending on the snow density. The multi-layer structure gives multiple reflections [12, 13]. Because of density contrasts between adjacent layers, giving rise to dielectric contrasts, total internal

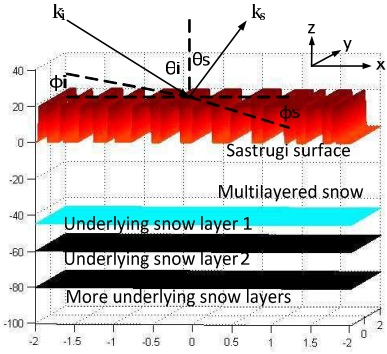

Figure 1. Typical profile of Sastrugi snow.

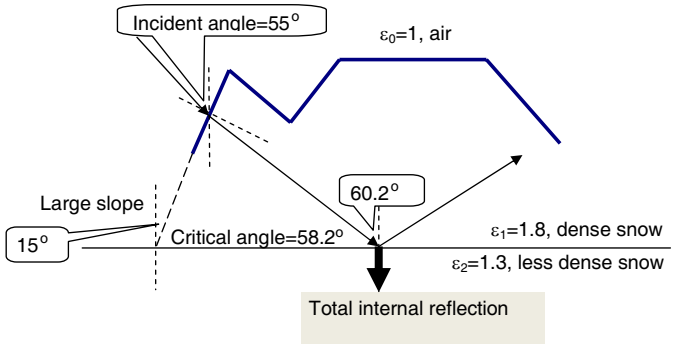

Figure 2. Scattering physics of total internal reflection.

reflection can occur at the layer interface depending on the incidence angle. The underlying scattering physics of Sastrugi surface overlying layered media are illustrated in Figure 2. Figure 2 shows a transmission angle of 60.2° inside the snow for an incident angle of 55° in air. Usually the angle of transmission inside snow is less than the incident angle in air. However the large slopes of the Sastrugi surface can facilitate a transmission angle in snow in this case that is larger than the incident angle in air. The large transmission angle in snow makes possible total internal reflection when the transmitted wave subsequently is incident on a layer with a smaller dielectric constant as shown in Figure 2. In this case shown in Figure 2, the large transmitted angle is larger than the critical angle for the interface separating dense snow from less dense snow resulting in total internal reflection. Total internal reflection will have different phase shifts for vertical and horizontal polarizations, thus creating nonzero results for both the third and the fourth Stokes parameters. Note that in Figure 2, 2-D scattering and transmission are shown rather than 3-D conical scattering, because the total internal reflection is the key issue to explain the scattering physics. However, 3-D conical scattering is considered in the following simulation.

We simulate Sastrugi roughness profiles based on the reported measured profiles [8]. The surface is to be composed of ridges. Since the Sastrugi surface is wind induced, we model it as one dimensional roughness along the direction of the prevailing wind. The surface generation procedure is described below.

The Sastrugi surface consists of ridges separated by grooves. Let L be the horizontal surface length, N be the number of ridges and $N + 1$ be the number of grooves. Also, let H be the height of the ridges and α be the maximal slope.

(1) We generate $2N+1$ random numbers in $[0,1]$: $\{a_1, a_2, \ldots, a_N\}$, $\{b_1, b_2, \ldots, b_{N+1}\}$.

(2) The horizontal length of the jth ridge is $a_j C_0$ $(j = 1, 2, \ldots, N)$ and horizontal length of the jth groove is $b_j C_0$ $(j = 1, 2, \ldots, N+1)$, where C_0 is to be determined below.

(3) To rise from a groove to a ridge of height H (Figure 3), we assume a gradual change of slope from zero to α, a region of constant slope α, and then from slope α gradually to zero slope.

(4) Let $\triangle l$ be the length discretization for this rise, and let $\{\theta_1, \theta_2, \ldots, \theta_m\}$ be the m angles increasing equidistantly from 0 to α. Thus for each $\triangle l$, the angle is $\theta_i\,(i = 1, 2, \ldots, m)$. Then the vertical rise distance for the gradual transition from 0 to α, is

$$S = \sum_{i=1}^{m} \triangle l \sin\theta_i \tag{1}$$

The corresponding horizontal stretch for this vertical rise is

$$C = \sum_{i=1}^{m} \triangle l \cos\theta_i \tag{2}$$

Then the angle stays at α and then gradually from α back to 0. Thus the vertical rise for the constant angle α is

$$H_{middle} = H - 2\sum_{i=1}^{m} \triangle l \sin\theta_i \tag{3}$$

(5) The corresponding horizontal length for the constant angle α is $\frac{H-2\sum_{i=1}^{m}\triangle l\sin\theta_i}{\tan\alpha}$. Thus the total horizontal stretch for the rise is $\frac{H-2\sum_{i=1}^{m}\triangle l\sin\theta_i}{\tan\alpha} + 2\sum_{i=1}^{m}\triangle l\cos\theta_i$. Note the factor of 2 is that in a rise from groove to a ridge, slope goes from 0 to α, stays at α, and then from α to 0. For the fall from ridge to groove, the same formula applies.

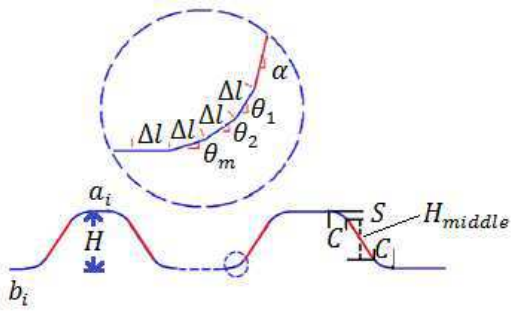

Figure 3. Fine structure of the random rough surface.

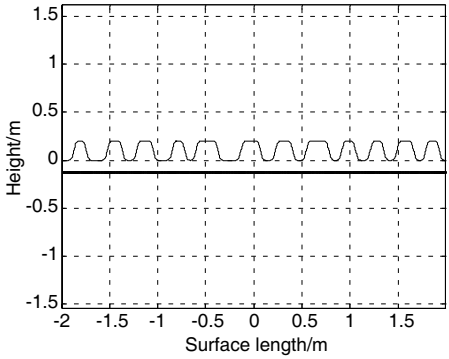

Figure 4. A randomly generated random Sastrugi surface profile $H = 20\,\text{cm}$, $\alpha = 75°$, $L = 4\,\text{m}$, $N = 12$, $\Delta l = 1.5\,\text{mm}$, $m = 16$.

Adding up the horizontal lengths of the ridges, grooves and the N horizontal lengths of the rise and fall give the equation for the total surface length L

$$C_0\left(\sum_{i=1}^{N} a_i + \sum_{i=1}^{N+1} b_i\right) + 2N\left[\frac{H - 2\sum_{i=1}^{m} \triangle l \sin\theta_i}{\tan\alpha} + 2\sum_{i=1}^{m} \triangle l \cos\theta_i\right] = L \tag{4}$$

Using Equation (4), we determine C_0. Then we go back to step 2 to determine the horizontal length of each ridge and groove. In Figure 4, we show a randomly generated profile based on the algorithm described.

3. BISTATIC REFLECTION AND TRANSMISSION COEFFICIENTS OF 4 STOKES PARAMETERS IN CONICAL DIFFRACTION BY SASTRUGI SURFACES

In this section, we formulate the problem of conical diffraction by Sastrugi surfaces. We first show the case of horizontal polarized incidence case. Then the formulation extended to general polarization of incidence.

3.1. Wave Equation and Surface Integral Equation

In conical scattering problem, the pilot field components of the wave equation are the transverse fields E_y and H_y

$$\begin{aligned} \left(\nabla_t^2 + k_t^2\right) E_y &= 0 \\ \left(\nabla_t^2 + k_t^2\right) H_y &= 0 \end{aligned} \tag{5}$$

where

$$\begin{aligned}\nabla_t &= \hat{x}\frac{\partial}{\partial x} + \hat{z}\frac{\partial}{\partial z}\\ k_t^2 &= k^2 - k_{iy}^2\\ k_{iy} &= k\sin\theta_i\,\sin\phi_i\end{aligned}$$

θ_i is the incident inclined angle and ϕ_i the incident azimuthal angle. Using extinction theorem, the surface integral equations corresponding to the wave equations can be obtained as

$$\begin{aligned}&E_{yi}(x,z) + \int_P ds'\left[E_y(x',z')\frac{\partial g}{\partial n'}(x,z;x',z')\right.\\ &\left.-g(x,z;x',z')\frac{\partial E_y}{\partial n'}(x,z;x',z')\right] = \frac{1}{2}E_y(x,z)\\ &H_{yi}(x,z) + \int_P ds'\left[H_y(x',z')\frac{\partial g}{\partial n'}(x,z;x',z')\right.\\ &\left.-g(x,z;x',z')\frac{\partial H_y}{\partial n'}(x,z;x',z')\right] = \frac{1}{2}H_y(x,z)\\ &-\int_P ds'\left[E_{1y}(x',z')\frac{\partial g_1}{\partial n'}(x,z;x',z')\right.\\ &\left.-g_1(x,z;x',z')\frac{\partial E_{1y}}{\partial n'}(x,z;x',z')\right] = \frac{1}{2}E_{1y}(x,z)\\ &-\int_P ds'\left[H_{1y}(x',z')\frac{\partial g_1}{\partial n'}(x,z;x',z')\right.\\ &\left.-g_1(x,z;x',z')\frac{\partial H_{1y}}{\partial n'}(x,z;x',z')\right] = \frac{1}{2}H_{1y}(x,z)\end{aligned} \tag{6}$$

where the subscript P for the integral sign denotes principal value, $g(x,z;x',z')$ and $g_1(x,z;x',z')$ denotes 2D Green's function in the incident and transmitted regions (with subscript 1), and $\frac{\partial}{\partial n'}$ denotes the normal derivative along the surface. The 2D Green's function are expressed in terms of Hankel function

$$\begin{aligned}g(x,z;x',z') &= \frac{i}{4}H_0^{(1)}\left(k_t\sqrt{(x-x')^2+(z-z')^2}\right)\\ g_1(x,z;x',z') &= \frac{i}{4}H_0^{(1)}\left(k_{1t}\sqrt{(x-x')^2+(z-z')^2}\right)\end{aligned} \tag{7}$$

Their normal derivatives are

$$\begin{aligned}\frac{\partial g}{\partial n'} &= \widehat{n_t'} \cdot \nabla' g = -\frac{ik_t}{4} H_1^{(1)}\left(k_t\sqrt{(x-x')^2+(z-z')^2}\right) \\ &\quad \frac{\frac{dz}{dx}(x-x')-(z-z')}{\sqrt{1+\left(\frac{dz}{dx}\right)^2}\sqrt{(x-x')^2+(z-z')^2}} \\ \frac{\partial g_1}{\partial n'} &= -\frac{ik_{1t}}{4} H_1^{(1)}\left(k_{1t}\sqrt{(x-x')^2+(z-z')^2}\right) \\ &\quad \frac{\frac{dz}{dx}(x-x')-(z-z')}{\sqrt{1+\left(\frac{dz}{dx}\right)^2}\sqrt{(x-x')^2+(z-z')^2}}\end{aligned} \tag{8}$$

We then impose the continuous boundary conditions of tangential electric and magnetic fields $E_y = E_{1y}$

$$\begin{aligned} H_y &= H_{1y} \\ \frac{\partial E_{1y}}{\partial n} &= \frac{k_{iy}}{\omega\varepsilon_1\sqrt{1+\left(\frac{dz}{dx}\right)^2}}\frac{dH_y}{dx}\left(\frac{k_{1t}^2}{k_t^2}-1\right)+\frac{k_{1t}^2\varepsilon}{k_t^2\varepsilon_1}\frac{\partial E_y}{\partial n} \\ \frac{\partial H_{1y}}{\partial n} &= -\frac{k_{iy}}{\omega\mu\sqrt{1+\left(\frac{dz}{dx}\right)^2}}\frac{dE_y}{dx}\left(\frac{k_{1t}^2}{k_t^2}-1\right)+\frac{k_{1t}^2}{k_t^2}\frac{\partial H_y}{\partial n}\end{aligned} \tag{9}$$

where $\frac{dz}{dx}$ denotes the slope of at the point on the rough surface. From the boundary condition, TE and TM are coupled so that E_y, H_y are coupled. Thus E_y, H_y are to be solved jointly. This is unlike the previous paper [7] where TE and TM are decoupled because the incidence plane is the xz plane. There are thus four unknowns: E_y, H_y, $\frac{\partial E_y}{\partial n}$, $\frac{\partial H_y}{\partial n}$.

3.2. Tapered Incident Field

Let the incident wave have $e^{ik_{iy}y}$ dependence. First we consider horizontal polarized incidence case, in which the tapered incident electric field is

$$\begin{cases} \overrightarrow{E_i} = \hat{h}E_{hi} = \hat{x}E_{xi} + \hat{y}E_{yi} \\ E_{xi} = -E_{hi}\sin\phi_i \\ E_{yi} = E_{hi}\cos\phi_i \end{cases} \tag{10}$$

Then the tapered incident wave is

$$E_{hi} = \exp\left\{ik(x\sin\theta_i\cos\phi_i + y\sin\theta_i\sin\phi_i - z\cos\theta_i) - \left(\frac{x+z\tan\theta_i\ \cos\phi_i}{g}\right)^2\right\} \tag{11}$$

where g is a tapering factor which generally ranges from $\frac{L}{10}$ to $\frac{L}{4}$, where L is the length of the surface profile. According to [9], such tapered conical incident wave is good approximation of plane wave to the order of $O(\frac{1}{kg\cos\theta_i})$. Therefore if the length of the surface profile is large enough, the error of the plane wave approximation is negligible. Magnetic field can be obtained as

$$\begin{cases} \overrightarrow{H_i} = \frac{1}{i\omega\mu}\nabla\times\overrightarrow{E_i} = \frac{1}{i\omega\mu}\left(-\hat{x}\frac{\partial E_{yi}}{\partial z} + \hat{y}\frac{\partial E_{xi}}{\partial z} + \hat{z}\left(\frac{\partial E_{yi}}{\partial x} - \frac{\partial E_{xi}}{\partial y}\right)\right) \\ H_{xi} = \frac{1}{i\omega\mu}\cos\phi_i E_{hi}\left(ik\cos\theta_i + \frac{2\tan\theta_i\cos\phi_i(x+z\tan\theta_i\cos\phi_i)}{g^2}\right) \\ H_{yi} = \frac{1}{i\omega\mu}\sin\phi_i E_{hi}\left(ik\cos\theta_i + \frac{2\tan\theta_i\cos\phi_i(x+z\tan\theta_i\cos\phi_i)}{g^2}\right) \end{cases} \quad (12)$$

The total incident power is

$$P^{inc} = \frac{1}{2}\int_{-\infty}^{\infty} dx\,\mathrm{Re}\left[(-\hat{z})\cdot\left(\overrightarrow{E_i}\times\overrightarrow{H_i}\right)\right]\Big|_{z=0} = \sqrt{2\pi}\frac{g}{4}\frac{k}{\omega\mu}\cos\theta_i \quad (13)$$

3.3. Basis Function and Matrix Equations

To solve the surface integral Equation (6) accurately, we use the rooftop basis function. The rooftop basis function $f_i(x)$ is defined on every two neighboring intervals $[x_{i-1}, x_i]$ and $[x_i, x_{i+1}]$

$$f_i(x) = \begin{cases} \frac{x-x_{i-1}}{x_i-x_{i-1}}, & x\in[x_{i-1},x_i] \\ \frac{x_{i+1}-x}{x_{i+1}-x_i}, & x\in[x_i,x_{i+1}] \\ 0, & x<x_{i-1} \text{ or } x>x_{i+1} \end{cases} \quad (14)$$

Then we convert the principal value integral into a finite sum, and write the integral Equation (6) in the form of a matrix Equation (15). Let the number of basis functions be N, so that there are a total of $4N$ unknowns. Then the matrix equations are

$$\begin{bmatrix} \overline{\overline{Z_{11}}}_{N\times N} & \overline{\overline{Z_{12}}}_{N\times N} & \overline{\overline{0}}_{N\times N} & \overline{\overline{0}}_{N\times N} \\ \overline{\overline{Z_{21}}}_{N\times N} & \overline{\overline{Z_{22}}}_{N\times N} & \overline{\overline{Z_{23}}}_{N\times N} & \overline{\overline{0}}_{N\times N} \\ \overline{\overline{0}}_{N\times N} & \overline{\overline{0}}_{N\times N} & \overline{\overline{Z_{33}}}_{N\times N} & \overline{\overline{Z_{34}}}_{N\times N} \\ \overline{\overline{Z_{41}}}_{N\times N} & \overline{\overline{0}}_{N\times N} & \overline{\overline{Z_{43}}}_{N\times N} & \overline{\overline{Z_{44}}}_{N\times N} \end{bmatrix} \begin{bmatrix} \overline{E_y}_{N\times 1} \\ \overline{H_y}_{N\times 1} \\ \overline{\partial E_y/\partial n}_{N\times 1} \\ \overline{\partial H_y/\partial n}_{N\times 1} \end{bmatrix}$$
$$= \begin{bmatrix} \overline{E_{yi}}_{N\times 1} \\ \overline{H_{yi}}_{N\times 1} \\ \overline{0}_{N\times 1} \\ \overline{0}_{N\times 1} \end{bmatrix} \quad (15)$$

The right-hand side is the incident field which can be obtained from Section 3.2. On the left-hand side, to evaluate the integral of the product of the rooftop basis function and the Hankel function we use

a 4-point Gauss-Legendre quadrature to calculate it. Then the non-diagonal elements ($m \neq n$) of the sub-matrices in the first and the second rows are

$$\begin{aligned}
Z_{11}(m,n) &= -\frac{ik_t}{8}\sum_{g=1}^{4} w_g \left(-\frac{z_n - z_{n-1}}{x_n - x_{n-1}}\left(x_m - x_g^{(1)}\right) + \left(z_m - z_g^{(1)}\right)\right) \\
&\quad \frac{H_1^{(1)}\left(k_t d_{mg}^{(1)}\right)}{d_{mg}^{(1)}}\left(x_g^{(1)} - x_{n-1}\right) \\
&\quad -\frac{ik_t}{8}\sum_{g=1}^{4} w_g \left(-\frac{z_{n+1} - z_n}{x_{n+1} - x_n}\left(x_m - x_g^{(2)}\right) + \left(z_m - z_g^{(2)}\right)\right) \\
&\quad \frac{H_1^{(1)}\left(k_t d_{mg}^{(2)}\right)}{d_{mg}^{(2)}}\left(x_{n+1} - x_g^{(2)}\right) \\
d_{mg}^{(1)} &= \sqrt{\left(x_m - x_g^{(1)}\right)^2 + \left(z_m - z_g^{(1)}\right)^2},\ g = 1,2,3,4 \\
x_g^{(1)} &= t_g \frac{x_n - x_{n-1}}{2} + \frac{x_{n-1} + x_n}{2}, \quad g = 1,2,3,4 \\
z_g^{(1)} &= \frac{z_n - z_{n-1}}{x_n - x_{n-1}}\left(x_g^{(1)} - x_{n-1}\right) + z_{n-1}, \quad g = 1,2,3,4 \\
d_{mg}^{(2)} &= \sqrt{\left(x_m - x_g^{(2)}\right)^2 + \left(z_m - z_g^{(2)}\right)^2}, \quad g = 1,2,3,4 \\
x_g^{(2)} &= t_g \frac{x_{n+1} - x_n}{2} + \frac{x_n + x_{n+1}}{2}, \quad g = 1,2,3,4 \\
z_g^{(2)} &= \frac{z_{n+1} - z_n}{x_{n+1} - x_n}\left(x_g^{(2)} - x_n\right) + z_n, \quad g = 1,2,3,4
\end{aligned}$$

where $w_g,\ t_g$ $(g = 1,2,3,4)$ are the weight and interpolation points of Gauss-Legendre quadrature.

$$\begin{aligned}
Z_{12}(m,n) =& \frac{i}{8}\sqrt{1+\left(\frac{z_n - z_{n-1}}{x_n - x_{n-1}}\right)^2}\sum_{g=1}^{4} w_g H_1^{(1)}\left(k_t d_{mg}^{(1)}\right)\left(x_g^{(1)} - x_{n-1}\right) \\
&+ \frac{i}{8}\sqrt{1+\left(\frac{z_{n+1} - z_n}{x_{n+1} - x_n}\right)^2}\sum_{g=1}^{4} w_g H_1^{(1)}\left(k_t d_{mg}^{(2)}\right)\left(x_{n+1} - x_g^{(2)}\right) \\
Z_{21}(m,n) =& \frac{ik_{1t}}{8}\sum_{g=1}^{4} w_g \left(-\frac{z_n - z_{n-1}}{x_n - x_{n-1}}\left(x_m - x_g^{(1)}\right) + \left(z_m - z_g^{(1)}\right)\right)
\end{aligned}$$

$$\frac{H_1^{(1)}\left(k_{1t}d_{mg}^{(1)}\right)}{d_{mg}^{(1)}}\left(x_g^{(1)}-x_{n-1}\right)+\frac{ik_{1t}}{8}\sum_{g=1}^{4}w_g\Big(-\frac{z_{n+1}-z_n}{x_{n+1}-x_n}$$

$$\left(x_m-x_g^{(2)}\right)+\left(z_m-z_g^{(2)}\right)\Big)\frac{H_1^{(1)}\left(k_{1t}d_{mg}^{(2)}\right)}{d_{mg}^{(2)}}\left(x_{n+1}-x_g^{(2)}\right)$$

$$Z_{22}(m,n)=-\frac{i}{8}\frac{k_{1t}^2\varepsilon_{r1}}{k_t^2}\sqrt{1+\left(\frac{z_n-z_{n-1}}{x_n-x_{n-1}}\right)^2}\sum_{g=1}^{4}w_gH_0^{(1)}\left(k_{1t}d_{mg}^{(1)}\right)$$

$$\left(x_g^{(1)}-x_{n-1}\right)-\frac{i}{8}\frac{k_{1t}^2\varepsilon_{r1}}{k_t^2}\sqrt{1+\left(\frac{z_{n+1}-z_n}{x_{n+1}-x_n}\right)^2}$$

$$\sum_{g=1}^{4}w_gH_0^{(1)}\left(k_{1t}d_{mg}^{(2)}\right)\left(x_{n+1}-x_g^{(2)}\right)$$

$$Z_{23}(m,n)=-\frac{i}{8}\frac{k_{iy}}{\omega\varepsilon_1}\left(\frac{k_{1t}^2}{k_t^2}-1\right)\sum_{g=1}^{4}w_gH_0^{(1)}\left(k_{1t}d_{mg}^{(1)}\right)$$

$$+\frac{i}{8}\frac{k_{iy}}{\omega\varepsilon_1}\left(\frac{k_{1t}^2}{k_t^2}-1\right)\int_{g=1}^{4}w_gH_0^{(1)}\left(k_{1t}d_{mg}^{(2)}\right) \tag{16}$$

The remaining matrix elements are the diagonal elements, or the 'self patch' which means the source point x_m and the field point x_n are in the same interval and will cause logarithm singularity. We use the small-argument asymptotic expression for Hankel function to solve this problem, therefore the final expressions are

$$Z_{11}(m,m)=\frac{1}{2}$$

$$Z_{21}(m,m)=\frac{1}{2}$$

$$Z_{12}(m,m)=\left(\frac{i}{8}-\frac{\gamma}{4\pi}+\frac{3}{8\pi}\right)\left((x_m-x_{m-1})\sqrt{1+\left(\frac{z_m-z_{m-1}}{x_m-x_{m-1}}\right)^2}\right.$$

$$\left.+(x_{m+1}-x_m)\sqrt{1+\left(\frac{z_{m+1}-z_m}{x_{m+1}-x_m}\right)^2}\right)-\frac{x_m-x_{m-1}}{4\pi}$$

$$\ln\left(\frac{k_t}{2}(x_m-x_{m-1})\sqrt{1+\left(\frac{z_m-z_{m-1}}{x_m-x_{m-1}}\right)^2}\right)\sqrt{1+\left(\frac{z_m-z_{m-1}}{x_m-x_{m-1}}\right)^2}$$

$$-\frac{x_{m+1}-x_m}{4\pi}\ln\left(\frac{k_t}{2}\left(x_{m+1}-x_m\right)\sqrt{1+\left(\frac{z_{m+1}-z_m}{x_{m+1}-x_m}\right)^2}\right)\sqrt{1+\left(\frac{z_{m+1}-z_m}{x_{m+1}-x_m}\right)^2}$$

$$Z_{22}\left(m,m\right)=\frac{k_{1t}^2\varepsilon_{r1}}{k_t^2}\left[-\left(\frac{i}{8}-\frac{\gamma}{4\pi}+\frac{3}{8\pi}\right)\right.$$

$$\left(\left(x_m-x_{m-1}\right)\sqrt{1+\left(\frac{z_m-z_{m-1}}{x_m-x_{m-1}}\right)^2}+\left(x_{m+1}-x_m\right)\sqrt{1+\left(\frac{z_{m+1}-z_m}{x_{m+1}-x_m}\right)^2}\right)$$

$$+\frac{x_m-x_{m-1}}{4\pi}\ln\left(\frac{k_{1t}}{2}\left(x_m-x_{m-1}\right)\sqrt{1+\left(\frac{z_m-z_{m-1}}{x_m-x_{m-1}}\right)^2}\right)\sqrt{1+\left(\frac{z_m-z_{m-1}}{x_m-x_{m-1}}\right)^2}$$

$$\left.+\frac{x_{m+1}-x_m}{4\pi}\ln\left(\frac{k_{1t}}{2}\left(x_{m+1}-x_m\right)\sqrt{1+\left(\frac{z_{m+1}-z_m}{x_{m+1}-x_m}\right)^2}\right)\sqrt{1+\left(\frac{z_{m+1}-z_m}{x_{m+1}-x_m}\right)^2}\right]$$

$$Z_{23}\left(m,m\right)=\frac{k_{iy}}{2\pi\omega\varepsilon_1}\left(\frac{k_{1t}^2}{k_t^2}-1\right)\ln\left(\frac{\left(x_m-x_{m-1}\right)\sqrt{1+\left(\frac{z_m-z_{m-1}}{x_m-x_{m-1}}\right)^2}}{\left(x_{m+1}-x_m\right)\sqrt{1+\left(\frac{z_{m+1}-z_m}{x_{m+1}-x_m}\right)^2}}\right) \tag{17}$$

where $\gamma\approx 0.577$ is the Euler constant. The surface integral equations for magnetic field are similar so that the sub-matrices on the third and fourth rows have similar forms as the first two rows

$$\begin{aligned}
\overline{\overline{Z_{33}}} &= \overline{\overline{Z_{11}}} \\
\overline{\overline{Z_{34}}} &= \overline{\overline{Z_{12}}} \\
\overline{\overline{Z_{41}}} &= -\frac{\varepsilon_1}{\mu_0}\overline{\overline{Z_{23}}} \\
\overline{\overline{Z_{43}}} &= \overline{\overline{Z_{21}}} \\
\overline{\overline{Z_{44}}} &= \frac{1}{\varepsilon_{r1}}\overline{\overline{Z_{22}}}
\end{aligned} \tag{18}$$

We used direct matrix inversion based on LU decomposition for this problem because of the large RMS heights. So far the largest scale of simulation we can run on a single-processor server is, that the number of rooftop basis function N is 8270 for each of the 4 unknowns. Thus, the size of the impedance Z matrix is 33080×33080. For each realization, it takes 45 minutes to run the simulation, and the memory usage is 17.0 GB. The server has Intel Xeon dual core E5620 processors.

3.4. Scattered and Transmitted Fields

After the surface unknowns are calculated, we use large-argument asymptotic expression for Hankel function, to obtain the bistatic scattered and transmitted fields.

Bistatic scattering:

$$\begin{aligned}
&\tilde{E}(\vartheta_s) = \int_S dx' \Big[E_y(x') jk_T\big(f'(x')\sin\vartheta_s - \cos\vartheta_s\big) \\
&-\sqrt{1+[f'(x')]^2}\frac{\partial E_y}{\partial n}(x')\Big]\exp\big(-jk_T x'\sin\vartheta_s - jk_T z'\cos\vartheta_s\big) \\
&\tilde{H}(\vartheta_s) = \int_S dx' \Big[H_y(x') jk_T\big(f'(x')\sin\vartheta_s - \cos\vartheta_s\big) \\
&-\sqrt{1+[f'(x')]^2}\frac{\partial H_y}{\partial n}(x')\Big]\exp\big(-jk_T x'\sin\vartheta_s - jk_T z'\cos\vartheta_s\big) \\
&E_{xs} = \frac{i}{4}\sqrt{\frac{2}{\pi k_T r}}\exp\Big(jk_T r - j\frac{\pi}{4}\Big)\Big(-\frac{k_{iy}}{k_t}\tilde{E}(\vartheta_s)\sin\vartheta_s + \eta\frac{k}{k_t}\tilde{H}(\vartheta_s)\cos\vartheta_s\Big) \\
&E_{ys} = \frac{i}{4}\sqrt{\frac{2}{\pi k_T r}}\exp\Big(jk_T r - j\frac{\pi}{4}\Big)\tilde{E}(\vartheta_s) \\
&E_{zs} = \frac{i}{4}\sqrt{\frac{2}{\pi k_T r}}\exp\Big(jk_T r - j\frac{\pi}{4}\Big)\Big(-\frac{k_{iy}}{k_t}\tilde{E}(\vartheta_s)\cos\vartheta_s - \eta\frac{k}{k_t}\tilde{H}(\vartheta_s)\sin\vartheta_s\Big) \\
&H_{ys} = \frac{i}{4}\sqrt{\frac{2}{\pi k_T r}}\exp\Big(jk_T r - j\frac{\pi}{4}\Big)\tilde{H}(\vartheta_s) \\
&dP_s = \frac{1}{16\pi}\frac{k}{k_T^2}\left[\frac{1}{\eta}\Big|\tilde{E}(\vartheta_s)\Big|^2 + \eta\Big|\tilde{H}(\vartheta_s)\Big|^2\right]d\vartheta_s
\end{aligned} \tag{19}$$

Bistatic transmission

$$\begin{aligned}
&\tilde{E}(\vartheta_t) = \int_S dx' \Big[E_{1y}(x') jk_{1T}\big(f'(x')\sin\vartheta_t + \cos\vartheta_t\big) \\
&-\sqrt{1+[f'(x')]^2}\frac{\partial E_{1y}}{\partial n}(x')\Big]\exp\big(-jk_{1T} x'\sin\vartheta_s + jk_{1T} z'\cos\vartheta_s\big) \\
&\tilde{H}(\vartheta_t) = \int_S dx' \Big[H_{1y}(x') jk_{1T}\big(f'(x')\sin\vartheta_t + \cos\vartheta_t\big) \\
&-\sqrt{1+[f'(x')]^2}\frac{\partial H_{1y}}{\partial n}(x')\Big]\exp\big(-jk_{1T} x'\sin\vartheta_t + jk_{1T} z'\cos\vartheta_t\big)
\end{aligned}$$

$$
\begin{aligned}
E_{xt} &= \frac{i}{4}\sqrt{\frac{2}{\pi k_{1T} r}}\exp\left(jk_{1T}r - j\frac{\pi}{4}\right)\left(-\frac{k_{iy}}{k_{1t}}\tilde{E}\left(\vartheta_t\right)\sin\vartheta_t - \eta_1\frac{k_1}{k_{1t}}\tilde{H}\left(\vartheta_t\right)\cos\vartheta_t\right)\\
E_{yt} &= \frac{i}{4}\sqrt{\frac{2}{\pi k_{1T} r}}\exp\left(jk_{1T}r - j\frac{\pi}{4}\right)\tilde{E}\left(\vartheta_t\right)\\
E_{zt} &= \frac{i}{4}\sqrt{\frac{2}{\pi k_{1T} r}}\exp\left(jk_{1T}r - j\frac{\pi}{4}\right)\left(\frac{k_{iy}}{k_{1t}}\tilde{E}\left(\vartheta_t\right)\cos\vartheta_t - \eta_1\frac{k_1}{k_{1t}}\tilde{H}\left(\vartheta_t\right)\sin\vartheta_t\right)\\
H_{yt} &= \frac{i}{4}\sqrt{\frac{2}{\pi k_{1T} r}}\exp\left(jk_{1T}r - j\frac{\pi}{4}\right)\tilde{H}\left(\vartheta_t\right)\\
dP_t &= \frac{1}{16\pi}\frac{k_1}{k_{1T}^2}\left[\frac{1}{\eta_1}\left|\tilde{E}\left(\vartheta_t\right)\right|^2 + \eta_1\left|\tilde{H}\left(\vartheta_t\right)\right|^2\right]d\vartheta_t
\end{aligned}
\tag{20}
$$

From the expressions of the three components of the electric field, we convert them into vertical and horizontal components, and obtain the corresponding Stokes parameters. Note that we simplify the conical scattering problem to a 2D problem by assuming $\exp(ik_{iy}y)$ dependence. Therefore the differential power above is a function of ϑ_s or ϑ_t. We next do angle conversion from these ϑ_s, ϑ_t to Ω_s, Ω_t or θ_s, ϕ_s, θ_t, ϕ_t as follows.

Bistatic scattering of θ_s, ϕ_s in terms of ϑ_s

$$
\begin{aligned}
&\cos\theta_s = \sqrt{1-(\sin\theta_i\sin\phi_i\ )^2}\cos\vartheta_s, \quad 0<\theta_i<\frac{\pi}{2},\\
&0<\phi_i<\pi, \quad -\frac{\pi}{2}<\vartheta_s<\frac{\pi}{2}, \quad 0<\theta_s<\frac{\pi}{2},\\
&\sin\phi_s = \frac{\sin\theta_i\sin\phi_i}{\sin\theta_s}, \quad 0<\phi_s<\pi,\\
&\phi_s = \pi - \arcsin\left(\frac{\sin\theta_i\ \sin\phi_i}{\sin\theta_s}\right), \quad \text{if } \vartheta_s<0.
\end{aligned}
\tag{21}
$$

Bistatic transmission of θ_t, ϕ_t in terms of ϑ_t

$$
\begin{aligned}
&\cos\theta_t = \sqrt{1-\frac{1}{\epsilon_r}(\sin\theta_i\sin\phi_i)^2}\cos\vartheta_t, \quad 0<\theta_i<\frac{\pi}{2},\\
&0<\phi_i<\pi, \quad -\frac{\pi}{2}<\vartheta_t<\frac{\pi}{2}, \quad 0<\theta_t<\frac{\pi}{2},\\
&\sin\phi_t = \frac{\sin\theta_i\sin\theta_i}{\sqrt{\epsilon_r}\sin\theta_t}, \quad 0<\phi_t<\pi,\\
&\phi_t = \pi - \arcsin\left(\frac{\sin\theta_i\ \sin\phi_i}{\sqrt{\epsilon_r}\sin\theta_t}\right), \text{ if } \vartheta_t<0.
\end{aligned}
\tag{22}
$$

Because of the conical scattering problem, there is only one

independent angular variable of θ and ϕ so that θ is in terms of ϕ and vice versa.

3.5. Scattering and Transmission Matrices

To build the 4-by-4 scattering and transmission matrices, vector wave equation is used and different polarized incident wave are imposed. For example, when the incident wave is horizontal polarization

$$\begin{aligned} \vec{E}^{inc} &= \hat{h} E_{hi} \\ \vec{E}^{sc} &= \hat{v} E_{vs} + \hat{h} E_{hs} \end{aligned} \tag{23}$$

Then E_{vi}, E_{vs} can be used to calculate the Stokes parameters and scattering matrix

$$\begin{aligned} & I_{vi} = 0,\ I_{hi} = \frac{|E_{hi}|^2}{\eta_i},\ U_i = 0,\ V_i = 0, \\ & I_{vs} = \frac{|E_{vs}|^2}{\eta_s}, \\ & I_{hs} = \frac{|E_{hs}|^2}{\eta_s}, \\ & U_s = \frac{2}{\eta_s} \mathrm{Re}\left(E_{vs} E_{hs}^*\right), \\ & V_s = \frac{2}{\eta_s} \mathrm{Im}\left(E_{vs} E_{hs}^*\right) \end{aligned} \tag{24}$$

$$\begin{bmatrix} I_{vs}(\theta_s) \\ I_{hs}(\theta_s) \\ U_s(\theta_s) \\ V_s(\theta_s) \end{bmatrix} = \left[\bar{\bar{R}}_{si}(\theta_s; \theta_i)\right]_{4\times 4} \begin{bmatrix} I_{vi}(\theta_i) \\ I_{hi}(\theta_i) \\ U_i(\theta_i) \\ V_i(\theta_i) \end{bmatrix} \tag{25}$$

First we use Equation (24) to calculate corresponding Stokes parameters; then consider the form of Equation (25), the second column of the 4-by-4 scattering matrix can be obtained from ratio of the scattered Stokes parameters to the incident Stokes parameters. Thus using horizontal polarized incidence, we obtain this second column. Other cases of incident polarization are discussed below.

(1) For vertical polarization

$$\begin{cases} \overrightarrow{E_i} = \hat{x}E_{xi} + \hat{y}E_{yi} + \hat{z}E_{zi} \\ E_{xi} = -\psi^{inc}\cos\theta_i\,\cos\phi_i \\ E_{yi} = -\psi^{inc}\cos\theta_i\,\sin\phi_i \\ E_{zi} = -\psi^{inc}\sin\theta_i \end{cases} \tag{26}$$

$$\overrightarrow{H_i} = \frac{1}{i\omega\mu}\nabla\times\overrightarrow{E_i}$$

$$P^{inc} = \frac{1}{2}\int_{-\infty}^{\infty} dx\,\mathrm{Re}\left(\overrightarrow{E_i}\times\overrightarrow{H_i}\right)\Big|_{z=0} = \sqrt{2\pi}\frac{g}{4}\frac{\kappa}{\omega\mu}\cos\theta_i$$

(2) For arbitrary linear combination of vertical and horizontal polarizations

$$\begin{cases} \overrightarrow{E_i} = \hat{x}E_{xi} + \hat{y}E_{yi} + \hat{z}E_{zi} \\ E_{xi} = -\psi^{inc}\left(\frac{1}{\sqrt{2}}\cos\theta_i\cos\phi_i + \frac{1}{\sqrt{2}}\exp\left(-i\beta\right)\sin\phi_i\right) \\ E_{yi} = \psi^{inc}\left(-\frac{1}{\sqrt{2}}\cos\theta_i\sin\phi_i + \frac{1}{\sqrt{2}}\exp\left(-i\beta\right)\cos\phi_i\right) \\ E_{zi} = -\frac{1}{\sqrt{2}}\psi^{inc}\sin\theta_i \end{cases} \tag{27}$$

$$\overrightarrow{H_i} = \frac{1}{i\omega\mu}\nabla\times\overrightarrow{E_i}$$

$$P^{inc} = \frac{1}{2}\int_{-\infty}^{\infty} dx\,\mathrm{Re}\left(\overrightarrow{E_i}\times\overrightarrow{H_i}\right)\Big|_{z=0} = \sqrt{2\pi}\frac{g}{4}\frac{k}{\omega\mu}\cos\theta_i$$

The term $\exp(-i\beta)$ is the phase difference between vertical and horizontal polarization. The incident power remains the same as other two types of polarization. By using 4 different kinds of polarized incidences, the bistatic reflection and transmission 4 by 4 matrices are constructed [5].

3.6. Bistatic Transmission Coefficients: Incident from Air onto Snow

Bistatic transmission coefficients from air to snow are shown in Figure 5. The parameters for Figure 5 are: frequency = 10.7 GHz; inclined incident angle = 55°; relative permittivity of snow = 1.6; height of ridges = 20 cm ($\sim$ 7.1 wavelengths). The numerical parameters are: surface length = 10 m ($\sim$ 356.7 wavelengths); number of ridges = 10.

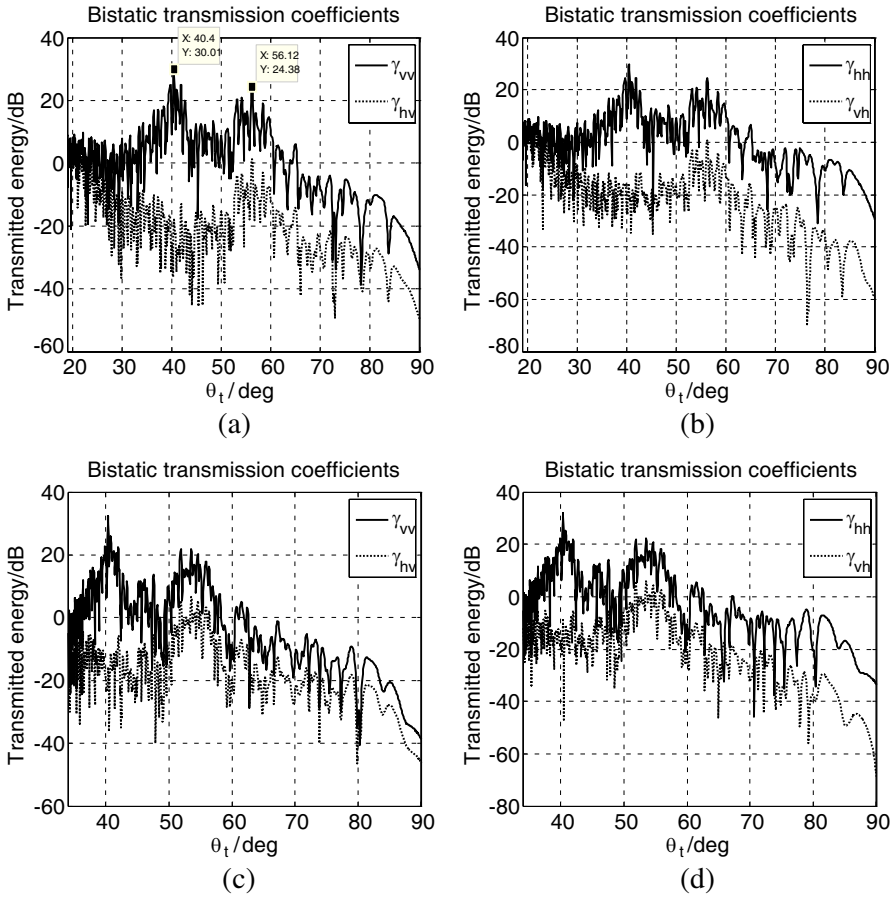

Figure 5. Bistatic transmission coefficients from air to snow. (a) Vertical polarization incidence; $\phi_i = 30°$; (b) Horizontal polarization incidence; $\phi_i = 30°$; (c) Vertical polarization incidence; $\phi_i = 60°$; (d) Horizontal polarization incidence; $\phi_i = 60°$.

In Figure 5(a), the co-polarization and cross-polarization for vertical incidence are shown. The solid line is co-polarization and the dotted line is the cross-polarization. They are averaged over 20 realizations. There is a transmission peak for transmission angle at 40.4°. This agrees with Snell's law of a flat surface.

$$\begin{aligned} &n_1 \sin\theta_i = n_2 \sin\theta_t \\ &\theta_i = 55.0°, \quad \theta_t = 40.4° \end{aligned} \tag{28}$$

The peak at 40.4° is the specular transmission direction. It also exists

in Figures 5(b) $\sim$ (d). Different azimuthal incident angles are used in Figure 5. These are useful as the observing directions of passive microwave remote sensing are at various azimuthal angles. Besides the specular transmission direction for a flat surface, there also exists other secondary transmission peaks between 50° and 60°. The magnitudes of these transmission peaks are about 5.6 dB ($\sim$ 0.28 times) lower than that of the specular transmission peak at 40.4°. These peaks are consequences of the large-slope section of the surface profile, as discussed in Section 1. Suppose the relative permittivity of the second snow layer is 1.1, the critical angle between the first two snow layers can be obtained as

$$\theta_c = \arcsin \frac{n_{snow2}}{n_{snow1}} = \arcsin \frac{\sqrt{1.1}}{\sqrt{1.6}} = 56.0^\circ \tag{29}$$

Therefore, the secondary peaks beyond 56° in Figure 5 will cause total internal reflection at the interface between the first snow layer and the second snow layer.

3.7. Bistatic Transmission Coefficients: Incident from Snow onto Air

Bistatic transmission coefficients from snow to air are shown in the Figure 6.

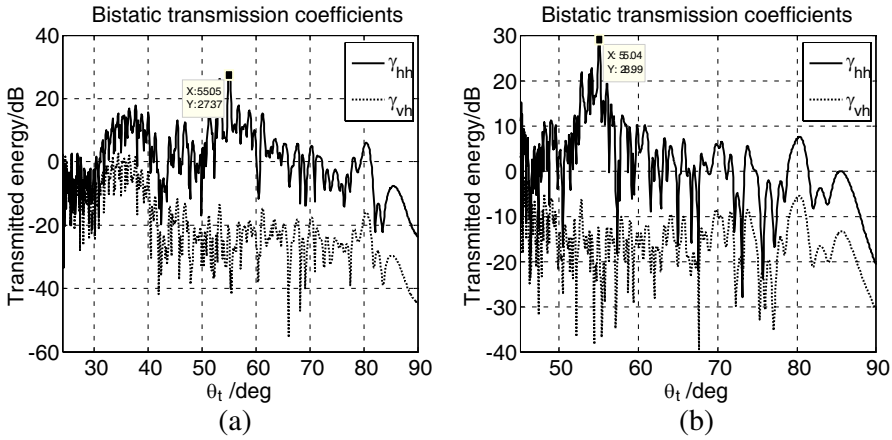

Figure 6. Bistatic coefficients of a Sastrugi surface: maximal slope = 62.5°. (a) Bistatic transmission coefficients: snow to air; $\theta_i = 40.4^\circ$; $\phi_t = 30^\circ$; 10.7 GHz; (b) Bistatic transmission coefficients: snow to air; $\theta_i = 40.4^\circ$; $\phi_t = 60^\circ$; 10.7 GHz.

The solid line is the co-polarization and the dotted line is the cross-polarization. Noting that the inclined incident angle is 40.4°, it is clear that the peaks at 55° are due to Snell's law for a flat surface. Horizontal incidence is shown in the figure. Vertical polarization has similar results.

3.8. Energy Conservation Check

The energy conservation check is

$$P_{v,h}^{inc} = P^{sc} + P^{tran} = \int d\Omega_s \left[P_{vs}\left(\theta_s, \phi_s\right) + P_{hs}\left(\theta_s, \phi_s\right)\right] + \int d\Omega_t \left[P_{vt}\left(\theta_t, \phi_t\right) + P_{ht}\left(\theta_t, \phi_t\right)\right] \tag{30}$$

The quantities $P_{vs}(\theta_s, \phi_s)$, $P_{hs}(\theta_s, \phi_s)$, $P_{vt}(\theta_t, \phi_t)$, $P_{ht}(\theta_t, \phi_t)$ can be obtained from the scattered and transmitted electric fields, while the incident power $P_{v,h}^{inc}$ are calculated for each case of incidence. The energy conservation check are within $99.0\% \sim 100.9\%$ for simulations in this paper.

4. VECTOR RADIATIVE TRANSFER EQUATIONS WITH ROUGH SURFACE BOUNDARY CONDITIONS

The radiative transfer equations are applied to the snow structure. The governing equations in the first snow layer are

$$\begin{aligned} \cos\theta \frac{d\bar{I}_u\left(\theta, z\right)}{dz} &= -\kappa_a \bar{I}_u\left(\theta, z\right) + \kappa_a T \varepsilon_r \bar{I}_0 \\ -\cos\theta \frac{d\bar{I}_d\left(\theta, z\right)}{dz} &= -\kappa_a \bar{I}_d\left(\theta, z\right) + \kappa_a T \varepsilon_r \bar{I}_0 \\ \bar{I}_0 &= [1\ 1\ 0\ 0]^t \end{aligned} \tag{31}$$

At each point in the random media, the Stokes parameters vector $\bar{I}\left(\theta, z\right)$ propagates in all directions $(0 < \theta < \pi)$, so it is convenient to divide $\bar{I}\left(\theta, z\right)$ into upward and downward going Stokes vectors [11]. In Equation (31), vector $\bar{I}_u\left(\theta, z\right)$ refers to the upward Stokes parameters vector which propagates in θ direction and locates at position z, while $\bar{I}_d\left(\theta, z\right)$ refers to the downward Stokes parameters vector which propagates in $\pi - \theta$ direction and locates at position z. $\bar{I}_0 = [1\ 1\ 0\ 0]^t$ is the thermal emission term, so its third and fourth components are incoherently averaged to zero. κ_a refers to the absorption coefficient, T refers to the physical temperature.

In the emission term, the constant factor $\frac{K}{\lambda_0^2}$ in the emission term is suppressed and can be re-inserted in the final results. In conical diffraction, there is only one single ϕ for every θ, as the two are related from Equations (21)–(22). Thus we will only show the θ dependence in the governing equations. The matrix forms of solutions are

$$\begin{aligned} \bar{I}_u(\theta, z) &= \bar{A}(\theta) \exp\left(-\kappa_a \sec\theta\,(z+d)\right) + T\varepsilon_r \bar{I}_0 \\ \bar{I}_d(\theta, z) &= \bar{B}(\theta) \exp\left(+\kappa_a \sec\theta z\right) + T\varepsilon_r \bar{I}_0 \end{aligned} \tag{32}$$

We assume that the interfaces of the subsurface snow layers are smooth. The rough surface boundary conditions are only for the Sastrugi interface. The boundary conditions at $z = -d$ is

$$\bar{I}_{u1}(\theta_1, z=-d) = \bar{\bar{R}}_{12}(\theta_1)\bar{I}_{d1}(\theta_1, z=-d) + \bar{\bar{T}}_{21}(\theta_2;\theta_1)\bar{I}_{u2}(\theta_2, z=-d) \tag{33}$$

where $-d$ is the position of the interface between the first and second snow layers. The subscript 1 or 2 refers to the first or second snow layer. For the interface of the Sastrugi surfaces, the radiative transfer equation has the roughness boundary condition as

$$\bar{I}_{d1}(\theta_1, z=0)\cos\theta_1 = \int d\theta_1' \sin\theta_1' \cos\theta_1' \bar{\bar{R}}_{10}(\theta_1';\theta_1)\bar{I}_{u1}(\theta_1', z=0) \tag{34}$$

In the above equations, $\bar{\bar{R}}_{12}(\theta_1)$ is the reflection matrix at the underlying interface, and can be extended to multilayer cases. $\bar{\bar{T}}_{21}(\theta_2;\theta_1)\,\bar{I}_{u2}(\theta_2, z=-d)$ is the thermal emission from the second snow layer. Reflection matrix $\bar{\bar{R}}_{10}(\theta_1';\theta_1)$ is the bistatic scattering coefficients at the Sastrugi rough surface.

After inserting the matrix forms of the solutions into the boundary conditions, the matrix equations are

$$\begin{aligned} &\left(\bar{B}(\theta_1) + T_1\varepsilon_{r1}\bar{I}_0\right)\cos\theta_1 \\ &= \int d\theta_1' \sin\theta_1' \cos\theta_1' \bar{\bar{R}}_{10}\left(\theta_1';\theta_1\right)\left(\bar{A}\left(\theta_1'\right)\exp\left(-\kappa_a \sec\theta_1' d\right) + T_1\varepsilon_{r1}\bar{I}_0\right) \\ &\bar{A}(\theta_1) + T_1\varepsilon_{r1}\bar{I}_0 \\ &= \bar{\bar{R}}_{12}(\theta_1)\left(\bar{B}(\theta_1)\exp(-\kappa_a \sec\theta_1 d) + T_1\varepsilon_{r1}\bar{I}_0\right) + \bar{\bar{T}}_{21}(\theta_2;\theta_1)\,T_2\varepsilon_{r2}\bar{I}_0 \\ &\bar{I}_0 = [1\ 1\ 0\ 0]^t \end{aligned} \tag{35}$$

Note that the snow layers have similar permittivity or that ε_{r1} is close to ε_{r2}. The upward going intensity are close to the physical temperature so that the coefficient $\bar{A}(\theta_1)$ is a small value compared to $\bar{B}(\theta_1)$. Therefore in thelowest order, the $\bar{A}(\theta_1)$ inside the integral is treated as zero. Thus, the vector radiative transfer equations with the boundary conditions can be solved in an iteration scheme.

(1) Lowest Order:

$$\begin{aligned}
&\bar{A}^{(0)}(\theta_1) = 0 \\
&\bar{B}^{(0)}(\theta_1) = \int d\theta_1' \sin\theta_1' \, \frac{\cos\theta_1'}{\cos\theta_1} T_1 \varepsilon_{r1} \bar{\bar{R}}_{10}(\theta_1'; \theta_1) \, \bar{I}_0 - T_1 \varepsilon_{r1} \bar{I}_0
\end{aligned} \tag{36}$$

(2) Iteration scheme: $n \geq 1$

$$\begin{aligned}
\bar{A}^{(n)}(\theta_1) =& \bar{\bar{R}}_{12}(\theta_1) \left(\bar{B}^{(n-1)}(\theta_1) \exp(-\kappa_a \sec\theta_1 \; d) + T_1 \varepsilon_{r1} \bar{I}_0 \right) \\
&+ \bar{\bar{T}}_{21}(\theta_2; \theta_1) \, T_2 \varepsilon_{r2} \bar{I}_0 - T_1 \varepsilon_{r1} \bar{I}_0 \\
\bar{B}^{(n)}(\theta_1) =& \int d\theta_1' \sin\theta_1' \, \frac{\cos\theta_1'}{\cos\theta_1} \bar{\bar{R}}_{10}(\theta_1'; \theta_1) \\
&\left(\bar{A}^{(n)}(\theta_1') \exp(-\kappa_a \sec\theta_1' \; d) + T_1 \varepsilon_{r1} \bar{I}_0 \right) - T_1 \varepsilon_{r1} \bar{I}_0
\end{aligned} \tag{37}$$

(3) Stopping criterion: We used the following criterion

$$\frac{\left\| \bar{A}^{(n)}(\theta_1) - \bar{A}^{(n-1)}(\theta_1) \right\|}{\left\| \bar{A}^{(n)}(\theta_1) \right\|} < 1\% \tag{38}$$

After the coefficient matrices are solved, we calculate the upward going Stokes parameters in the air region

$$\begin{aligned}
\bar{I}_{u0}(\theta_0) =& \int d\theta_1' \sin\theta_1' \frac{\cos\theta_1'}{\cos\theta_1} \bar{\bar{T}}_{10}(\theta_1'; \theta_0) \bar{I}_{u1}(\theta_1', z=0) = \int d\theta_1' \sin\theta_1' \\
&\frac{\cos\theta_1'}{\cos\theta_1} \bar{\bar{T}}_{10}(\theta_1'; \theta_0) \left(\bar{A}^{(n)}(\theta_1') \exp(-\kappa_a \sec\theta_1' d) + T \varepsilon_{r1} \bar{I}_0 \right)
\end{aligned} \tag{39}$$

$$\bar{I}_0 = [1 \; 1 \; 0 \; 0]^t$$

For typical simulation cases (parameters shown in the next section), the iteration scheme requires 15 steps to satisfy the stopping criterion Equation (38). From the 2nd iteration, the ratio $|\bar{A}(\theta)/\bar{B}(\theta)|$ will remain stable at 5.80%, which validates the premise of the iteration scheme.

5. RESULTS OF FOUR STOKES PARAMETERS

In this section, we illustrate numerical results of the partial coherent approach for the two frequencies 10.7 GHz and 18.7 GHz. The input parameters are:

(1) Inclined incident angle = 55°;
(2) Physical parameters of Sastrugi surface

- Height of ridges = 20 cm;
- Largest slope = 62.5°;

(3) Numerical parameters of Sastrugi surface
- Finite surface length = 10 m;
- Number of ridges = 10;
- Tapered factor = 4;

(4) Physical parameters of the layered structure
- Number of layers = 2;
- Permittivity of layers = 1.6, 1.3;
- Physical temperatures of layers = 270 K, 260 K;
- Thickness of the first layer ($\varepsilon_r = 1.6$) = 15 cm;

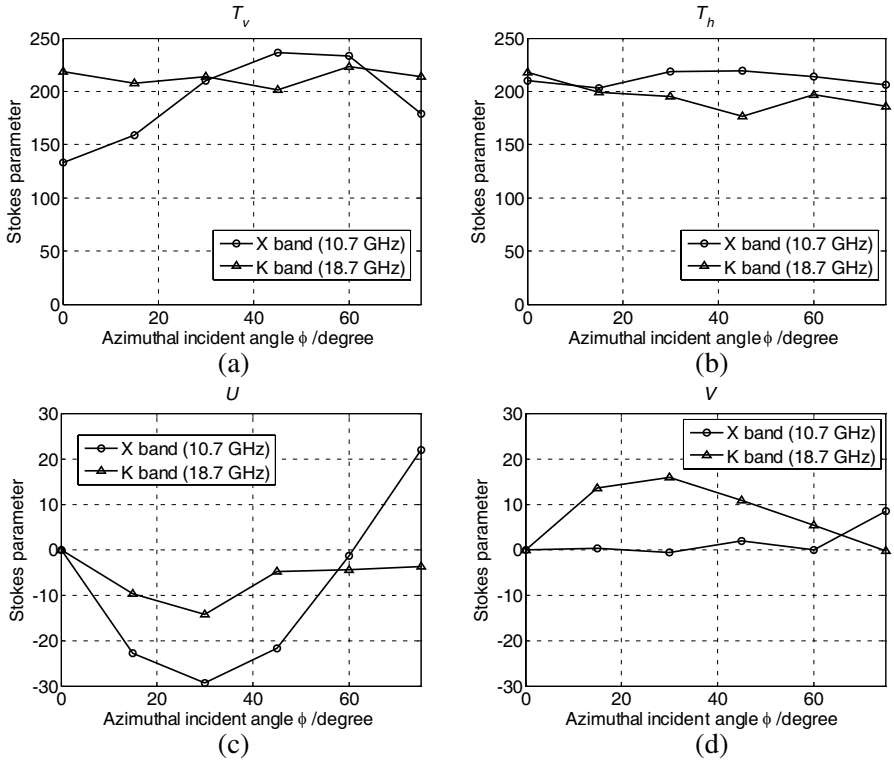

Figure 7. 4 Stokes parameters for two frequency 10.7 GHz and 18.7 GHz. (a) Vertical polarization brightness temperature: T_v; (b) Horizontal polarization brightness temperature: T_h; (c) Real part of polarization correlation: U; (d) Imaginery part of polarization correlation: V.

(5) Numerical parameters of the layered structure
   – Absorption coefficient = 0.05;

Figure 7 shows the four Stokes parameters versus the azimuthal incident angle, which is the angle in the horizontal plane between the satellite observation direction and the direction of roughness. In each figure, results for the two frequencies are compared.

The brightness temperatures T_v and T_h are around 200 K, which are slightly lower than the experimental data, but nevertheless are comparable to experimental data. These lowering of brightness temperatures can be attributed to multiple reflections and internal reflections. The third and fourth Stokes parameters range from −30 K to 20 K, which are large values. These large values of third and fourth Stokes parameters contain much information on the anisotropic structure. We note that such large values of third and fourth Stokes parameters exist in both frequencies, which show that the effects can be attributed to geometric optics. This is in contrast to volume scattering of small particles which are strongly frequency dependent [4, 5, 14].

6. CONCLUSION

In this paper, a hybrid method, composed of surface integral equation method and radiative transfer theory, is proposed to solve all the four Stokes parameters for the snow structures in Greenland area, where Sastrugi surfaces and multilayer snow structure exist. The surface integral equation with conical incident wave is solved by method of moments, and the radiative transfer equation is applied to a two-layer snow structure. The bistatic transmission coefficients show that a large height and large slope surface can create large transmission angle, even larger than the critical angle at the underlying interface. The results of Stokes parameters agree with the experimental data, which validates the hybrid method. The results do not have the coherent fluctuations that were in the full wave solution [6] for the multilayer snow structure. The third and fourth Stokes parameters are large when total internal reflection occurs, and their magnitudes are comparable for X band and Ku band. Future studies will include volume scattering in snow in addition to the multiple reflections from layer boundaries [14–16].

ACKNOWLEDGMENT

The work is supported by National Science Foundation under grant No. 0713863.

REFERENCES

1. Li, L., P. Gaiser, M. R. Albert, D. G. Long, and E. M. Twarog, "WindSat passive microwave polarimetric signatures of the greenland ice sheet," *IEEE Transactions on Geoscience and Remote Sensing*, Vol. 46, No. 9, 2622–2631, Sep. 2008.
2. Yueh, S. H., W. J. Wilson, S. J. Dinardo, and S. V. Hsiao, "Polarimetric microwave wind radiometer model function and retrieval testing for WindSat," *IEEE Transactions on Geoscience and Remote Sensing*, Vol. 44, 584–596, Mar. 2006.
3. Johnson, J. T., R. Shin, L. Tsang, K. Pak, and J. A. Kong, "A numerical study of ocean polarimetric thermal emission," *IEEE Trans. Geosci. Remote Sens.*, Vol. 37, No. 1, 8–20, 1999.
4. Tsang, L., "Thermal emission of nonspherical particles," *Radio Sci.*, Vol. 19, No. 4, 966–974, 1984.
5. Tsang, L., "Polarimetric passive microwave remote sensing of random discrete scatterers and rough surfaces," *Journal of Electromagnetic Waves and Applications*, Vol. 5, No. 1, 41–57, 1991.
6. Tsang, L., P. Xu, and K. S. Chen, "Third and fourth stokes parameters in polarimetric passive microwave remote sensing of rough surfaces over layered media," *Microwave and Optical Technology Letters*, Vol. 50, No. 12, 3063–3069, Dec. 2008.
7. Liang, D., P. Xu, L. Tsang, Z. Gui, and K.-S. Chen, "Electromagnetic scattering by rough surfaces with large heights and slopes with applications to microwave remote sensing of rough surface over layered media," *Progress In Electromagnetics Research*, Vol. 95, 199–218, 2009.
8. Albert, M. R. and R. L. Hawley, "Seasonal changes in snow surface roughness characteristics at Summit, Greenland: Implications for snow and firn ventilation," *Annals of Glaciology*, Vol. 35, No. 1, 510–514, Jan. 2002.
9. Li, L., C. H. Chan, and L. Tsang, "Numerical simulation of conical diffraction of tapered electromagnetic waves from random rough surfaces and applications to passive remote sensing," *Radio Sci.*, Vol. 29, No. 3, 587–598, 1994.
10. Tsang, L., J. A. Kong, K. H. Ding, and C. O. Ao, *Scattering of Electromagnetic Waves, Vol. 2: Numerical Simulations*, Wiley Interscience, 2001.
11. Tsang, L., J. A. Kong, and K. H. Ding, *Scattering of Electromagnetic Waves, Theories and Applications*, Wiley-Interscience, 2000.

12. West, R., D. P. Winebrenner, L. Tsang, and H. Rott, "Microwave emission from density stratified Antarctic firn at 6 cm, wavelength," *Journal of Glaciology*, Vol. 42, No. 140, 63–76, 1996.
13. Chang, W. and L. Tsang, "Conical electromagnetic waves diffraction from sastrugi type surfaces of layered snow dunes on greenland ice sheets in passive microwave remote sensing," *IEEE International Geoscience and Remote Sensing Symposium (IGARSS)*, 122–125, Jul. 24–29, 2011.
14. Tsang, L., M. C. Kubacsi, and J. A. Kong, "Radiative transfer theory for active remote sensing of a layer of ellipsoidal scatterers," *Radio Sci.,* Vol. 16, No. 3, 321–329, May–Jun. 1981.
15. Tsang, L., C. T. Chen, A. T. C. Chang, J. Guo, and K. H. Ding, "Dense media radiative transfer theory based on quasicrystalline approximation with application to passive microwave remote sensing of snow," *Radio Sci.*, Vol. 35, No. 3, 731–749, May–Jun. 2000.
16. Ding, K. H., X. Xu, and L. Tsang, "Electromagnetic scattering by bicontinuous random microstructures with discrete permittivities," *IEEE Trans. Geosci. Remote Sens.,* Vol. 48, No. 8, 3139–3151, Aug. 2010.